



The University of  
**Nottingham**

UNITED KINGDOM · CHINA · MALAYSIA

Wong, Kelvin and Briddon, Stephen J. and Holliday, Nicholas D. and Kerr, Ian D. (2016) Plasma membrane dynamics and tetrameric organisation of ABCG2 transporters in mammalian cells revealed by single particle imaging techniques. *Biochimica et Biophysica Acta - Molecular Cell Research*, 1863 (1). pp. 19-29. ISSN 0006-3002

**Access from the University of Nottingham repository:**

[http://eprints.nottingham.ac.uk/34239/1/BBAMCR\\_17690-corrected.pdf](http://eprints.nottingham.ac.uk/34239/1/BBAMCR_17690-corrected.pdf)

**Copyright and reuse:**

The Nottingham ePrints service makes this work by researchers of the University of Nottingham available open access under the following conditions.


This article is made available under the Creative Commons Attribution Non-commercial No Derivatives licence and may be reused according to the conditions of the licence. For more details see: <http://creativecommons.org/licenses/by-nc-nd/2.5/>

**A note on versions:**

The version presented here may differ from the published version or from the version of record. If you wish to cite this item you are advised to consult the publisher's version. Please see the repository url above for details on accessing the published version and note that access may require a subscription.

For more information, please contact [eprints@nottingham.ac.uk](mailto:eprints@nottingham.ac.uk)

## AUTHOR QUERY FORM

 ELSEVIER	<b>Journal: BBAMCR</b>  <b>Article Number: 17690</b>	<b>Please e-mail your responses and any corrections to:</b>  <b>E-mail: <a href="mailto:Corrections.ESCH@elsevier.spitech.com">Corrections.ESCH@elsevier.spitech.com</a></b>
---	--	--

Dear Author,

Please check your proof carefully and mark all corrections at the appropriate place in the proof (e.g., by using on-screen annotation in the PDF file) or compile them in a separate list. Note: if you opt to annotate the file with software other than Adobe Reader then please also highlight the appropriate place in the PDF file. To ensure fast publication of your paper please return your corrections within 48 hours.

For correction or revision of any artwork, please consult <http://www.elsevier.com/artworkinstructions>.

We were unable to process your file(s) fully electronically and have proceeded by

Scanning (parts of) your article

Rekeying (parts of) your article

Scanning the artwork

Any queries or remarks that have arisen during the processing of your manuscript are listed below and highlighted by flags in the proof. Click on the 'Q' link to go to the location in the proof.

Location in article	<b>Query / Remark: <a href="#">click on the Q link to go</a></b> <b>Please insert your reply or correction at the corresponding line in the proof</b>
<a href="#">Q1</a>	The word "protein" was deleted here. Please check if appropriate.
<a href="#">Q2</a>	Your article is registered as a regular item and is being processed for inclusion in a regular issue of the journal. If this is NOT correct and your article belongs to a Special Issue/Collection please contact <a href="mailto:r.mathew@elsevier.com">r.mathew@elsevier.com</a> immediately prior to returning your corrections.
<a href="#">Q3</a>	Please confirm that given names and surnames have been identified correctly. <div style="border: 1px solid black; padding: 5px; margin: 10px auto; width: fit-content;">             Please check this box if you have no corrections to make to the PDF file. <input type="checkbox"/> </div>

Thank you for your assistance.



Contents lists available at ScienceDirect

## Biochimica et Biophysica Acta

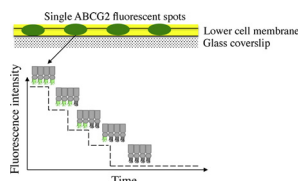
journal homepage: [www.elsevier.com/locate/bbamcr](http://www.elsevier.com/locate/bbamcr)

## Graphical abstract

**Plasma membrane dynamics and tetrameric organisation of ABCG2 transporters in mammalian cells revealed by single particle imaging techniques**

pp. xxx – xxx

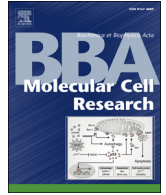
Kelvin Wong, Stephen J. Briddon, Nicholas D. Holliday, Ian D. Kerr\*





Contents lists available at ScienceDirect

## Biochimica et Biophysica Acta

journal homepage: [www.elsevier.com/locate/bbamcr](http://www.elsevier.com/locate/bbamcr)

## Highlights

**Plasma membrane dynamics and tetrameric organisation of ABCG2 transporters in mammalian cells revealed by single particle imaging techniques***Biochimica et Biophysica Acta xxx (2015) xxx – xxx*

Kelvin Wong, Stephen J. Briddon, Nicholas D. Holliday, Ian D. Kerr\*

*Cell Signalling Research Group, School of Life Sciences, Queen's Medical Centre, University of Nottingham, NG7 2UH, UK*

- ABCG2 is a half transporter predicted to oligomerise for function.
- We used single particle fluorescence methods to ascertain ABCG2's oligomeric state.
- Photon counting histogram analysis indicates ABCG2 forms tetramers.
- Stepwise photobleaching methods validate predominantly tetrameric structure of ABCG2.
- Inhibition of ABCG2 oligomerisation may therefore be a future therapeutic strategy.

Supplementary Fig. S1 Effects of binning time on the distributions of photon counting histogram (PCH) analysis. PCH distributions (red dots) of an example GFP-ABCG2 data set, fitted against the two-component PCH model (black dotted lines) using the binning times as indicated. 1 ms was chosen as the binning time for subsequent analysis to ensure appropriate photon counts (e.g. not fewer than 10 or higher than 200) were detected in the PCH analysis.

Supplementary Fig. S2 Comparison of free GFP and tandem GFP-GFP validates PCH analysis of particle molecular brightness. Data were obtained using one-component PCH analysis in Zen 2010, and are presented as mean  $\pm$  S.E.M. from at least 25 cells transiently expressing the respective proteins over 3 independent experiments.

Supplementary Fig. S3 Determination of the most appropriate model for PCH analysis. (A) Reduced  $\chi^2$  values obtained for CD86-GFP, CD28-GFP, and GFP-ABCG2 data sets using single-component (1-comp) or two-component (2-comp) PCH analysis in Zen 2010. Two-component PCH model improved the fitting of CD28 and ABCG2 data sets, as reduced  $\chi^2$  values were closer to one compared to single-component PCH model. However it did not improve the fitting of CD86-GFP data sets in which no difference was observed in the reduced  $\chi^2$  values. (B) Two-component PCH analysis did not identify a different component for CD86-GFP as no difference was observed in the molecular brightness (mean  $\pm$  S.E.M.) and component fraction (mean  $\pm$  S.E.M.) of component 1 (C1) and component 2 (C2). Data were collected from at least 30 cells over 4 independent experiments.

Supplementary Fig. S4 Determination of the most appropriate single oligomeric model for GFP-ABCG2. Various binomial fits assuming 10% spot overlap (lines and symbols) were compared against actual GFP-ABCG2 photobleaching step frequency histograms (hatched boxes) using a goodness of fit test (equation 5, section 2.6; Table 1). Dimer, trimer, tetramer and pentamer models of GFP-ABCG2 were generated, with probability of fluorescent GFP, pGFP, (set at 0.50 (panel A), 0.55 (B) or 0.60 (C)). Tetramer models in all three panels represented the best fit to the photobleaching data (Table 1).

Supplementary Movie 1 Stepwise photobleaching of GFP-ABCG2. The lower membrane of a HEK293T cell expressing GFP-ABCG2 at low level was illuminated using TIRF 22 configuration and photobleached at high power laser. TIFF video shows a complete 40 s recording sample at 20 frames per second.



## Q2 Plasma membrane dynamics and tetrameric organisation of ABCG2 transporters in mammalian cells revealed by single particle imaging techniques

Q3 Kevin Wong, Stephen J. Briddon, Nicholas D. Holliday, Ian D. Kerr\*

Cell Signalling Research Group, School of Life Sciences, Queen's Medical Centre, University of Nottingham, NG7 2UH, UK

### ARTICLE INFO

#### Article history:

Received 31 July 2015

Received in revised form 17 September 2015

Accepted 6 October 2015

Available online xxxxx

#### Keywords:

Abcg2

Oligomerisation

Fluorescence correlation spectroscopy

Photon counting histogram

Total internal reflection fluorescence

Stepwise photobleaching

### ABSTRACT

ABCG2 is one of three human ATP binding cassette (ABC) transporters involved in the export from cells of a chemically and structural diverse range of compounds. This multidrug efflux capability, together with a broad tissue distribution in the body, means that ABCG2 exerts a range of effects on normal physiology such as kidney urate transport, as well as contributing towards the pharmacokinetic profiles of many exogenous drugs. The primary sequence of ABCG2 contains only half the number of domains required for a functioning ABC transporter and so it must oligomerise in order to function, yet its oligomeric state in intact cell membranes remains uncharacterized. We have analysed ABCG2 in living cell membranes using a combination of fluorescence correlation spectroscopy, photon counting histogram analysis, and stepwise photobleaching to demonstrate a predominantly tetrameric structure for ABCG2 in the presence or absence of transport substrates. These results provide the essential basis for exploring pharmacological manipulation of oligomeric state as a strategy to modulate ABCG2 activity in future selective therapeutics.

© 2015 Published by Elsevier B.V.

### 1. Introduction

Eukaryotic multidrug efflux pumps have physiological relevance in metabolite and xenobiotic export, in cancer multidrug efflux and in influencing pharmacokinetics profiles of other pharmaceutical drugs. In humans, at least three members of the ATP binding cassette (ABC<sup>1</sup>) transporter superfamily are capable of multidrug efflux – ABCB1 (P-glycoprotein), ABCC1 (multidrug resistance protein-1) and ABCG2 (breast cancer resistance protein) [1]. The polypeptide chains of ABCB1 and ABCC1 contain the four core domains expected for a functional ABC transporter [2], i.e. two nucleotide-binding domains (NBDs) and two (or three in the case of ABCC1) transmembrane domains (TMDs). ABCG2's primary sequence is different in two significant respects, which make any structural inferences from our knowledge of other ABC transporters difficult [3]. Firstly, the protein has a single NBD and a single TMD in the polypeptide, leading it to be known as a “half-

transporter” [4]. Secondly these domains are in the “reverse order” compared to the majority of ABC transporters, with the NBD being N-terminal and the TMD being C-terminal.

Having only half the number of domains required for a functional ABC transporter has led to the assertion that ABCG2 must *at least* dimerise in order to function. Knowledge of its oligomeric state is therefore an essential element in our understanding of ABCG2 function.

To date, however, biochemical and structural analyses of ABCG2 have presented conflicting evidence of its oligomeric organisation. Dimer, tetramer, octamer and dodecamer formation of ABCG2 molecules have all been suggested [5–7], but these studies have often been limited by the need to extract ABCG2 from its membrane environment. Whilst oligomerisation of ABCG2 has been demonstrated in whole cells using FRET (fluorescence resonance energy transfer) or BiFC (bimolecular fluorescence complementation) microscopy [8,9], neither of these techniques are able to distinguish between dimers and higher order oligomerisation. There is, therefore, a pressing need to address ABCG2 stoichiometry in the intact membrane context, not only to improve understanding of the functional basis of this transporter family, but also to open up new pathways to selective inhibitor development, which target ABCG2 protein-protein interactions [10], instead of its less selective drug binding sites [11].

With this ambition in mind, two fluorescence techniques have been increasingly used to determine membrane protein oligomerisation in mammalian cells, with potential to resolve higher order protein complexes. The first, fluorescence correlation spectroscopy (FCS),

\* Corresponding author.

E-mail addresses: [nicholas.holliday@nottingham.ac.uk](mailto:nicholas.holliday@nottingham.ac.uk) (N.D. Holliday), [ian.kerr@nottingham.ac.uk](mailto:ian.kerr@nottingham.ac.uk) (I.D. Kerr).

<sup>1</sup> Abbreviations: ABC – ATP binding cassette; AOTF – acousto-optic tunable filters; BiFC – bimolecular fluorescence complementation; EMCCD – electron multiplying charge couple device; FCS – fluorescence correlation spectroscopy; FRAP – fluorescence recovery after photobleaching; FRET – fluorescence resonance energy transfer; GFP – green fluorescent protein; HEK – human embryonic kidney; MX – mitoxantrone; NBD – nucleotide binding domain; PBS – phosphate buffered saline; PCH – photon counting histogram; TIRF – total internal reflection fluorescence; TMD – transmembrane domain.



records fluorescence fluctuations generated by the diffusion of the fluorescently-tagged protein through a stationary confocal volume, illuminating a focal point of  $\sim 0.2 \mu\text{m}^2$  on the membrane [12]. Analysis of the fluctuation records with respect to mean amplitude, rather than time, generates a photon counting histogram (PCH) [13], from which the molecular brightness of the fluorescence particles can be derived to indicate oligomerisation [14–16]. In the second, single fluorescent particles are resolved using total internal reflection fluorescence (TIRF) imaging, which provides improved resolution of the lower plasma membrane fluorescent complexes by limiting the depth of excitation field ( $\sim 100 \text{ nm}$ ). The amplitudes of these particles are monitored over time in response to high intensity illumination, and the bleaching of individual subunits within the complex is detected as a series of discrete steps. This analysis was recently established as a valuable tool to determine the subunit composition of membrane proteins expressed in *Xenopus laevis* oocytes [17–19] and mammalian cells [20–23].

In the current study, we apply both FCS/PCH and stepwise photobleaching approaches to determine the membrane dynamics and oligomeric state of GFP-tagged ABCG2 expressed in human origin HEK293T cells. These data from independent fluorescence techniques provide novel evidence demonstrating tetrameric organisation of GFP-ABCG2 **in situ** in whole cells.

## 2. Materials and methods

### 2.1. Molecular biology and cell culture

An enhanced GFP template containing additional “superfolder” mutations M135T, V163A, S30R, and Y30N [24], and the A206K mutation to prevent fluorescent protein dimerisation [25] was employed. The GFP sequence was inserted in frame at the N-terminus of the ABCG2 cDNA in pcDNA3.1zeo (Invitrogen, Paisley, UK; [8]), using *XhoI* and *XbaI* restriction sites. CD28 and CD86 were amplified from vectors kindly provided by Professor Simon Davis (University of Oxford, UK) with *BamHI/XhoI* (CD86) or *EcoRI/XhoI* (CD28) flanking restriction sites, and stop codon removal. Both CD28 and CD86 had C-terminal truncations (at residue arginine 185 and arginine 277 respectively) to avoid potential cytoplasmic interactions that could affect the oligomeric behaviour of the controls [26]. Digested PCR products were inserted into pcDNA3.1zeo containing GFP between *XhoI/XbaI*, creating CD28-GFP or CD86-GFP fusion protein cDNAs. The tandem GFP-GFP construct contained two repeated GFP cDNAs joined in frame by a two-amino acid linker (Leu-Glu, *XhoI* site). The identities of all constructs were confirmed by DNA sequencing.

HEK293T cell passaging and transfection protocols were as described [8]. Stable cell lines expressing CD28-GFP, CD86-GFP or GFP-ABCG2 were selected using 200  $\mu\text{g}/\text{ml}$  zeocin for 10–15 days until healthy colonies were observed, and subsequently maintained at 40  $\mu\text{g}/\text{ml}$  zeocin. Mixed populations were also diluted cloned and screened for GFP fluorescence, to allow selection of low expressing cell lines (FCS/PCH and TIRF studies), through intensity comparisons under identical acquisition conditions.

### 2.2. Mitoxantrone accumulation assay

Stable, mixed population HEK293T cells expressing GFP-ABCG2 were seeded on poly-L-lysine coated 96-well plates (655,090, Greiner Bio-One, Stonehouse, UK). When confluent, cells were incubated with 4  $\mu\text{M}$  mitoxantrone (MX; Sigma-Aldrich, Poole, UK) alone, or in the presence of ABCG2 inhibitor, 1  $\mu\text{M}$  Ko143 [27] Sigma-Aldrich), for 0–60 min. Following fixation with 4% paraformaldehyde in PBS (10 min, room temperature), cell nuclei were counterstained with Hoechst 33,342 (Invitrogen, 2  $\mu\text{g}/\text{ml}$  in PBS). Cell images were acquired (4 sites per well) using an ImageXpress Micro plater reader (Molecular Devices, Wokingham, UK), equipped with a 20 $\times$  Nikon extra-long working distance air objective and standard DAPI (nucleus stain

detection), FITC (GFP detection), and Cy5 (MX detection) filter sets as described previously [8]. Average cellular MX fluorescence intensities were calculated by analysing the fluorescence images using the Multi-wavelength Cell Scoring analysis in MetaXpress 5.3 software (Molecular Devices, Wokingham, UK). Data are presented as an average % of MX accumulation (normalised against the highest fluorescence intensities obtained in each experiments) over time in the presence or absence of Ko143.

### 2.3. Fluorescence correlation spectroscopy (FCS) and photon counting histogram analysis (PCH)

Low expressing stable (CD86-GFP, CD28-GFP, and GFP-ABCG2) or transiently transfected (GFP and tandem GFP-GFP) cells were seeded and grown on poly-L-lysine coated Nunc LabTek 8-well chambered cover glasses. Cells were washed with Hank's balanced salt solution (HBSS) twice and allowed to equilibrate to 22 °C. For FCS measurements acquired on a Confocor 2 (Carl Zeiss GmbH, Jena, Germany), the confocal volume was positioned at the upper plasma membrane of the cells by performing a z-scan at low 488 nm Argon laser power ( $\sim 0.05 \text{ kW}/\text{cm}^2$ ). FCS measurements used 0.25  $\text{kW}/\text{cm}^2$  laser power in a single acquisition divided into 3  $\times$  15 s traces, after a 10 s pre-bleach with 0.60  $\text{kW}/\text{cm}^2$ . Emitted fluorescence was collected via a 505–550 nm bandpass filter. Cells with <100 kHz average fluorescence intensity were selected to produce autocorrelation decay curves. The autocorrelation function  $G(\tau)$  was calculated by considering fluorescence intensity fluctuations ( $\delta I$ ) from mean intensity  $\langle I \rangle$ , using Eq. (1) – comparing time-points at time  $t$  and  $t + \tau$  for a range of  $\tau$  values. For cytoplasmic GFP and tandem GFP-GFP, autocorrelation curves were fitted using a one-component 3D model (Eq. (2)). For the membrane proteins ABCG2, CD86 and CD28, autocorrelation curves were fitted with a two-component 2D diffusion models (Eq. (3)), with a fast autocorrelation component ( $\tau_{D1} \sim 200\text{--}400 \mu\text{s}$ ) assumed to be a product of FP photophysics [28,29]. This allowed derivation of the number ( $N$ ) and dwell times ( $\tau_D$ ) of the fluorescent particles within the confocal volume. A pre-exponential term (not shown in Eqs. (2) and (3) but described in [28]) was also used to describe other high frequency autocorrelation component (1–10  $\mu\text{s}$ ) arising from fluorophore photophysics.

$$G(\tau) = 1 + \frac{\langle \delta I(t) \cdot \delta I(t + \tau) \rangle}{\langle I \rangle^2} \quad (1)$$

$$G(\tau) = 1 + A \frac{1}{N} \left( 1 + \frac{\tau}{\tau_D} \right)^{-1} \left( 1 + \frac{\tau}{S^2 \tau_D} \right)^{-0.5} \quad (2)$$

$$G(\tau) = 1 + A \frac{1}{N} \left( F_1 \left( 1 + \frac{\tau}{\tau_{D1}} \right)^{-1} + F_2 \left( 1 + \frac{\tau}{\tau_{D2}} \right)^{-1} \right) \quad (3)$$

Autocorrelation curves were only analysed if they reached a clear asymptote as  $G(\tau)$  approached 1; typically this key criteria in FCS analysis rejects measurements affected by low frequency random movement of plasma membrane, photobleaching during acquisition, or large aggregates of fluorescent particles diffusing through the confocal detection volume. On each experimental day Rhodamine 6G (20 nM) calibration experiments were performed prior to cellular measurements to determine the radius of the confocal volume ( $r$ ) of the 488 nm laser employed for the excitation of GFP, as described previously [29]. From this assessment of the confocal radius  $r$ , diffusion coefficients ( $D$ ) of the membrane localised fusion proteins were estimated using  $\tau_{D2}$ , according to  $D = r^2/4\tau_{D2}$ .

PCH analysis was performed on all the FCS traces accepted for autocorrelation analysis, using single-component (for GFP, tandem GFP-GFP, CD86-GFP) or two-component (for CD28-GFP, GFP-ABCG2) PCH models. These models derived an additional estimate of the number of

198 fluorescent particles for each component ( $N$ ) within the volume, and estimated the molecular brightness ( $\epsilon$ ) of each component. In order to account for deviations in the shape of the Gaussian observation volume as a consequence of single photon excitation, a first order correction factor (typically 0.15–0.17) was estimated based on Rhodamine 6G calibration for the day's experiment [30]. An optimised binning time of 1 ms for generation of the PCH histogram (Fig. S1) was chosen to exclude the fast autocorrelation component due to GFP photophysics [29], while ensuring appropriate counts for a single bin. This binning time of choice also ensures that the membrane proteins of interest ( $\tau_{D2}$  of  $> 10$  ms) remained within the detection volume for the duration of the sampling period, a key assumption in PCH analysis [31]. PCH analysis, using one or two component models, was performed in Zen 2010 (Carl Zeiss).

212 Pooled data are presented as mean  $\pm$  S.E.M. for  $n$  cells; the number of independent experiments is also indicated where appropriate. Differences between data sets were assessed for significance using non-parametric Kruskal–Wallis analysis followed by Dunn's multiple comparisons post-test in GraphPad Prism 6.0 (GraphPad software, San Diego, CA, USA).

#### 218 2.4. Fluorescence recovery after photobleaching (FRAP)

219 GFP-ABCG2 mixed population cells were seeded on MatTek glass bottom dishes (thickness 0.16–0.19 mm and refractive index of 1.523), and media replaced by phenol-red free HBSS immediately prior to imaging. FRAP was performed on a LSM 710 confocal microscope (Carl Zeiss) using a 63 $\times$  Plan-Apochromat 1.4 NA M27 oil immersion objective. For image acquisition, 488 nm Argon laser excitation (2% power for normal acquisition; 100% and 30 iterations for photobleaching) was employed for the excitation of GFP and emission was collected at 493–598 nm. For FRAP experiments, cells were first left to equilibrate at 37 °C on the heated stage, 10 images of the cells (lower plasma membrane) were then acquired (512  $\times$  512 pixels; 1 s/scan), before a circular region of interest (ROI; radius,  $r = 2 \mu\text{m}$ ) was photobleached and FRAP recovery was monitored for 50 s.

232 Diffusion coefficients and mobile fractions were obtained from the FRAP experiments as previously described [29]. Briefly, FRAP recovery curves were fitted to data corrected for background and representative ROIs (Zen 2010), using a one phase exponential  $I(t) = I_0 - I_1 e^{-t/T_1}$ .  $I_0$  is the end value of recovered fluorescence intensity,  $I_1$  is the amplitude of the recovered fraction, and half time  $t_{1/2}$  is obtained from  $T_1$  by  $t_{1/2} = -T_1 \ln 0.5$ . The mobile fraction percentage was estimated by  $F1 = 100 * I_1 / (I_0 - I_A)$ , where  $I_0$  is the initial fluorescence intensity and  $I_A$  is the intensity immediately post bleach. As for FCS measurements, diffusion coefficients ( $D$ ) were also obtained by  $D = r^2 / 4 t_{1/2}$ . Pooled data are presented as mean  $\pm$  S.E.M. for  $n$  cells collected over a number of experiments, as indicated where appropriate.

#### 244 2.5. TIRF imaging

245 For single particle imaging, low expressing clonal lines were first seeded on poly-L-lysine coated MatTek dishes (as above) and fixed with 4% paraformaldehyde in PBS for 10 min., following 30 min treatment (37 °C) with 4  $\mu\text{M}$  MX or vehicle if required. The lower plasma membrane of the cell was illuminated under TIRF configuration using a 488 nm TIRF laser to produce an excitation field depth of approximately 100 nm. TIRF angles of 62–65° as indicated in the TIRF slider of the software (Zen 2012, Zeiss) were employed. GFP emission was collected using an emission bandpass filter 510–542 nm. For cell selection, 4% acousto-optic tunable filters (AOTF) laser excitation was employed and the display range of the EMCCD camera (QuantEM 512 from Photometrics, Tucson, AZ, USA) was adjusted to allow selection of low expressing cells. TIRF photobleaching videos were recorded at 10 Hz for 80 s at high laser power, 80% AOTF. Videos obtained as .zvi files were converted to 8-bit .tif files using LSM 5 Image Browser and ImageJ [32].

#### 260 2.6. Stepwise photobleaching analysis with binomial oligomeric models

261 The automated PIF algorithm developed in MATLAB (MathWorks, Natick, MA, USA) kindly provided by Dr. Rikard Blunck (Université de Montréal, Canada) was employed to analyse the photobleaching characteristics of single particle spots identified in the TIRF videos. The parameters for the analysis were chosen as described or recommended in [21]. Briefly, fluorescence intensities (arbitrary units, A.U.) of the fluorescent spots were calculated from a region of 5  $\times$  5 pixels, by fitting the total initial fluorescence intensity of each spot to a 2D Gaussian profile and subtracting the base line (estimated from the last 20 frames of recording) from the total intensities. A proximity threshold was employed to ensure that fluorescent spots accepted for analysis were free of neighbouring spots when the Gaussian profile had reached 20% of its maximum.

274 Following automated spot detection, the background intensity within the individual particle fluorescence traces was removed using a Laplacian of Gaussian (LoG) kernel-type file incorporated within the PIF algorithm. Photobleaching steps within the filtered traces were detected using an iterative process using repetitive assessment of the intensities averaged over short time segments. This process ensured that photobleaching steps were separated from the background noise or any blinking event of GFP in the intensity traces (see [21] for a detailed description). The minimum step to noise ratio (SNR) threshold was set at 1.6. The lower threshold compared to a previous study [21] is a consequence of not applying a Chung-Kennedy (CK) filter to the data to increase the fluorescence signal. The SNR threshold of 1.6 ensured that sufficient traces were accepted whilst maintaining the accuracy of the detection algorithm, as shown in [21]. Cells with  $> 20\%$  traces accepted were included in the final presentation as frequency histograms of the number of photobleaching steps observed, with the number of cells and experiments indicated where appropriate.

292 For the interpretation of photobleaching step frequency histograms, single oligomeric models were first generated using equation (4), in which the probability of observing  $x$  photobleaching steps is predicted based on the probability of individual GFP molecules within the complex being fluorescent ( $p$ ) and the highest oligomeric stoichiometry expected ( $n$ ).

$$(x; n, p) = \frac{n!}{x!(n-x)!} * p^x * (1-p)^{n-x} \quad (4)$$

299 We also assumed 10% overlapping fluorescent spots, modelled by the proportionate addition of a second binomial component, using  $2 \times n$  as the highest number oligomeric state. For example for a tetramer model, 10% of the total fluorescent spots obtained were modelled with  $n = 8$ , whilst the remaining 90% were with  $n = 4$ . The final predicted frequencies for  $x$  were calculated by summing the expected frequencies for the two binomial distributions.

306 A combined dimer/tetramer model was also employed to fit the frequency histograms. This model was calculated on a similar basis, in which expected frequencies were obtained by summations of dimer and tetramer distributions in appropriate proportions. The goodness of fit for the different models was assessed by calculation of the reduced chi<sup>2</sup> values ( $\chi^2$ ) using equation (5), where  $O$  = observed frequencies,  $E$  = expected frequencies, and  $n$  = highest number of photobleaching steps expected from the combined binomial distributions.

$$\chi^2 = \frac{\left[ \sum_n \frac{(O-E)^2}{E} \right]}{(n-1)} \quad (5)$$



### 3. Results

#### 3.1. GFP-tagged ABCG2 is targeted to the membrane and retains mitoxantrone transport function

N-terminal GFP-tagged ABCG2 was stably expressed in HEK293T cells in all studies, and used in comparison to transfected cell lines

expressing a range of controls – including cytoplasmic GFP or tandem GFP-GFP, and the transmembrane proteins CD86-GFP (monomeric control; [33–35]) or CD28-GFP (oligomer control; [34,36,37]). For all tagged proteins the same variant of GFP was used, containing monomeric and superfolder mutations (see 2.1). All proteins were expressed at the expected molecular weights, and the plasma membrane localisation of GFP-ABCG2, CD28-GFP and CD86-GFP in the mixed transfected

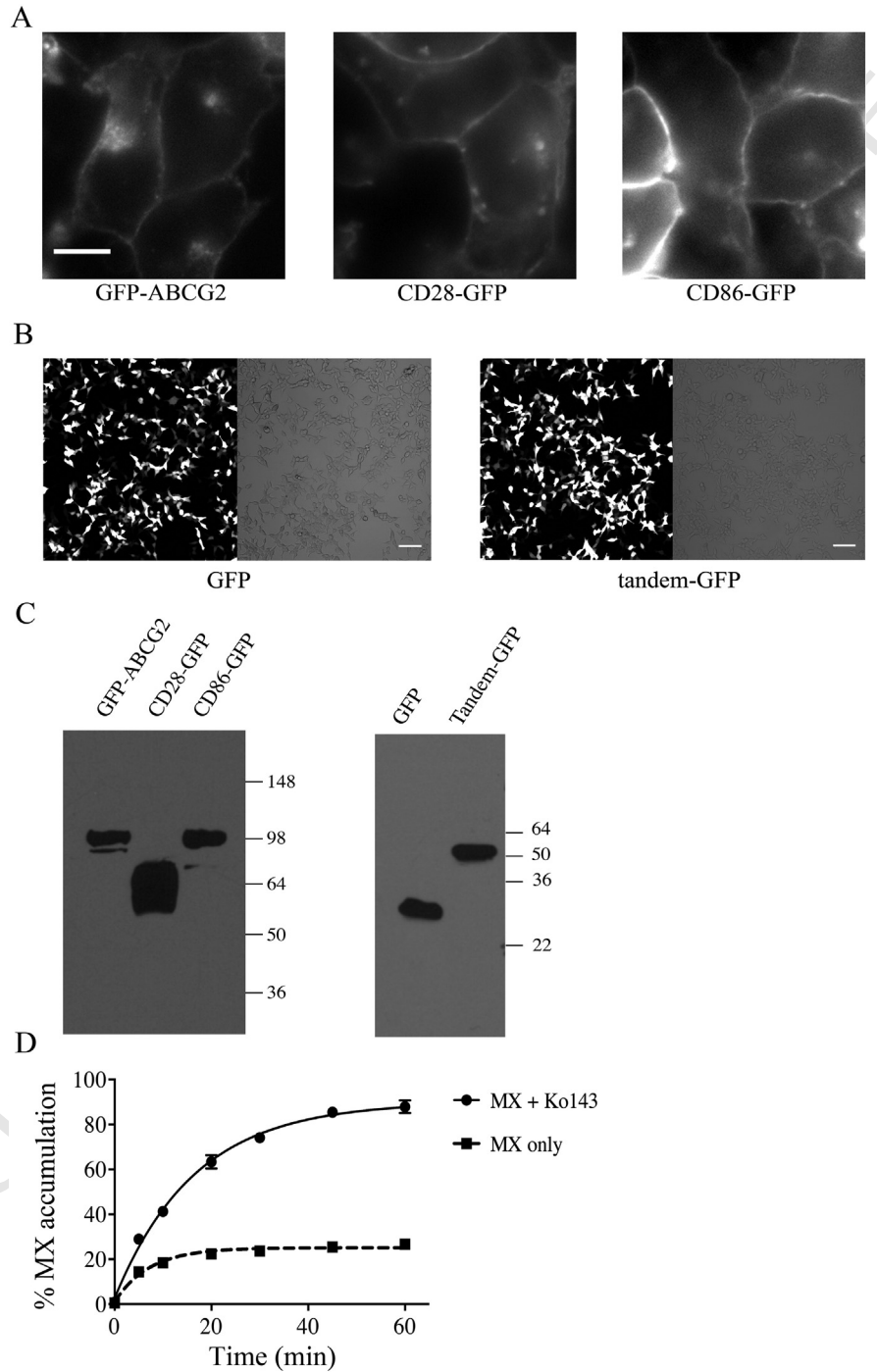


**Fig. 1.** Expression, localisation and function of fluorescent constructs when expressed in fixed HEK293T cells. (A) Membrane localisation of GFP-ABCG2, CD28-GFP, and CD86-GFP were confirmed by fluorescence imaging, representative images shown for at least 4 independent experiments. Scale bar = 10  $\mu$ m. (B) Cytoplasmic localisation of GFP and tandem-GFP. Scale bar = 100  $\mu$ m. (C) Western blot analysis of GFP-fusion proteins. Twenty micrograms (whole cell lysate) of membrane-localised proteins (left hand panel, 8% w/v acrylamide) or cytoplasmic proteins (right hand panel, 12% w/v acrylamide) were resolved by SDS-PAGE. All proteins were detected with mouse monoclonal anti-GFP antibodies and horseradish peroxidase conjugated secondary antibodies. (D) Increased accumulation of mitoxantrone (4  $\mu$ M MX) in the presence of ABCG2 inhibitor (1  $\mu$ M Ko143) demonstrated functional GFP-ABCG2 in HEK293T cells. Data were pooled from four independent experiments (at least 20,000 cells were analysed) and presented as mean  $\pm$  S.D.

328 populations was confirmed using fluorescence imaging (Fig. 1A–C).  
 329 Previous reports indicate that N-terminal tagging of ABCG2 does  
 330 not impact upon function [8] and this was demonstrated by showing

that that export of the fluorescence substrate mitoxantrone from 331  
 GFP-ABCG2 cells was prevented by the selective ABCG2 inhibitor 332  
 Ko143 (Fig. 1D). 333

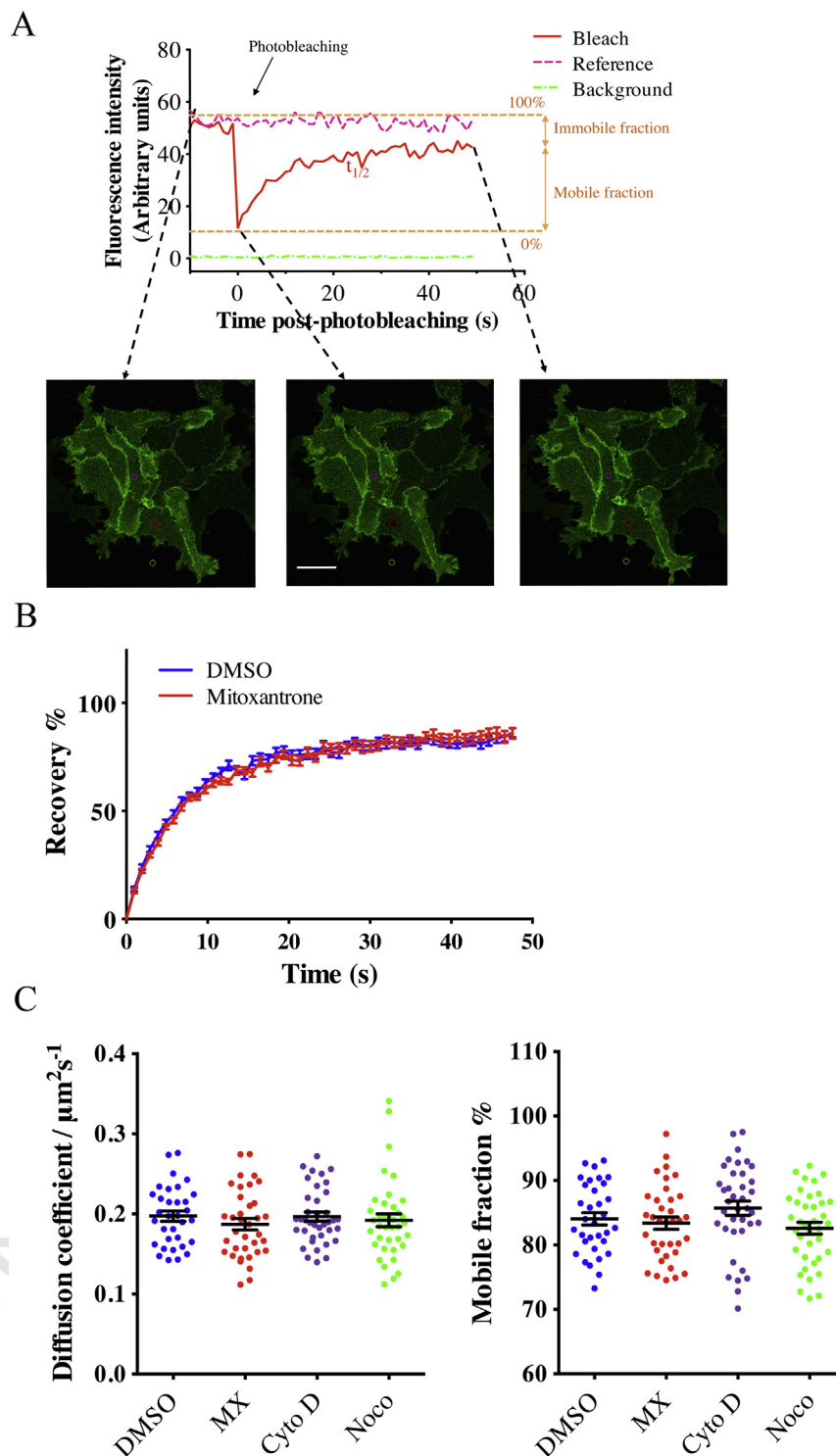


**Fig. 2.** FRAP measurements demonstrate that GFP-ABCG2 lateral mobility is unaffected by transport substrate or pharmacological manipulation of the cytoskeleton. (A) representative FRAP experiment, using the mixed population GFP-ABCG2 cell line, showing the fluorescence intensities of the bleach region of interest (ROI, 2  $\mu\text{m}$  radius, red circles), reference region (purple circle), and background region (green circle). The confocal images of lower plasma membrane of the cells at 3 different time points (before, immediately after, and 50 s after photobleaching) together with the respective regions indicated in the same colour are shown. The fluorescence intensities of the reference and background regions were used for correction of the ROI intensities in Zen 2010. Scale bar = 20  $\mu\text{m}$ . Kinetic parameters, e.g. time required for 50% recovery ( $t_{1/2}$ ) and mobile fraction were obtained using the corrected recovery curve, as described in Section 2.4 (B) Pooled and normalised recovery data comparing GFP-ABCG2 cells pretreated with vehicle (0.02% v/v DMSO) or 4  $\mu\text{M}$  mitoxantrone for at least 30 min (C) Summary histograms indicating the calculated GFP-ABCG2 diffusion coefficients and % mobile fraction following pre-incubation with vehicle, 4  $\mu\text{M}$  mitoxantrone (MX), 1  $\mu\text{M}$  nocodazole (Noco) or 1  $\mu\text{M}$  cytochalasin D (Cyto D) for at least 20 min. Bar and errors represent the mean  $\pm$  S.E.M. of the individual cell data points. All pooled data shown are combined from analysis of 33–38 cells in 3 independent experiments.

### 3.2. Diffusion of GFP-tagged proteins investigated by fluorescence recovery after photobleaching and fluorescence correlation spectroscopy

Initial measurements of GFP-ABCG2 lateral mobility were made using FRAP analysis of single living cells from the mixed stable HEK293T cell lines. Fluorescence recovery was monitored over 50 s following bleaching of a 2  $\mu\text{m}$  radius circular ROI within the lower plasma membrane (Fig. 2A), and these traces were sufficiently fitted with a single phase exponential assuming single component diffusion (Fig. 2B). These experiments demonstrated that GFP-ABCG2 was predominantly a mobile species (82.4  $\pm$  0.7% in the mobile fraction,  $n = 59$  cells from 3 experiments), with the half-time for recovery yielding an estimate of its diffusion co-efficient  $D$  as 0.18  $\pm$  0.00  $\mu\text{m}^2 \text{s}^{-1}$ . The presence of substrate (4  $\mu\text{M}$  mitoxantrone), or of disruptors of tubulin (1  $\mu\text{M}$  nocodazole) or actin (1  $\mu\text{M}$  cytochalasin D) did not alter diffusion coefficient or % mobile fraction significantly (Fig. 2C).

Lateral mobilities of the various GFP-tagged proteins were then analysed by recording fluorescence fluctuations over time using FCS measurements, with the stationary confocal volume positioned on the upper plasma membrane, using low expressing clonal cell lines (Figs. 3A and B). In comparison to FRAP, these measurements are restricted to mobile particles only (since immobile proteins do not generate time-dependent intensity fluctuations), and to the much smaller membrane region illuminated by the confocal volume ( $\sim 0.2 \mu\text{m}^2$ ). For membrane localised GFP-ABCG2, and the single pass transmembrane protein controls CD28-GFP and CD86-GFP, autocorrelation analysis used a two-component 2D model (Fig. 3C), in which dwell time  $\tau_{D1}$  (200–400  $\mu\text{s}$ ) was assumed to be a photophysical component [27,28] and  $\tau_{D2}$  was thus representative of the diffusion

of the tagged protein. From this parameter, a diffusion coefficient was derived of 0.11  $\pm$  0.03  $\mu\text{m}^2 \text{s}^{-1}$  for GFP-ABCG2, 2.4–2.6 fold slower than for CD28-GFP (0.27  $\pm$  0.10  $\mu\text{m}^2 \text{s}^{-1}$ ) or CD86-GFP (0.29  $\pm$  0.09  $\mu\text{m}^2 \text{s}^{-1}$ ; data were collected from at least 30 cells from 4 experiments). Thus despite the very different spatial scales used for FCS and FRAP assessments, the derived values of GFP-ABCG2  $D$  were within a 2-fold difference. Mobilities of the tagged membrane proteins were in turn 100 fold slower than those for cytoplasmic free GFP (35.6  $\pm$  5.1  $\mu\text{m}^2 \text{s}^{-1}$ ) or tandem GFP-GFP (21.3  $\pm$  3.7  $\mu\text{m}^2 \text{s}^{-1}$ ), in this case calculated via a single component 3D autocorrelation model (more than 25 cells, three experiments).

### 3.3. PCH analysis supports oligomerisation of ABCG2 in live cells

While the slow mobility of GFP-ABCG2 could suggest oligomeric complexes, molecular weight alone has a relatively minor influence on diffusion coefficients, in comparison to other factors that might restrict diffusion in the plasma membrane [38]. For example when considering otherwise unrestricted diffusion, a 2 fold change in  $D$  would only be predicted following an 8 fold change in molecular mass. However PCH analysis, which instead considers fluctuations around the mean intensity amplitude within FCS records, provides a means to directly estimate the molecular brightness ( $\epsilon$ ) of fluorescent particles within the confocal volume – and this should be directly proportional to the number of GFP molecules within the fluorescent complex. This method thus has greater potential to resolve ABCG2 stoichiometry in living cells. As described in 2.3, an optimised trace bin time of 1 ms was used to divide FCS recordings, and the frequency of bins containing different numbers of photon counts ( $k$ ) was the basis for construction of the PCH histogram. The

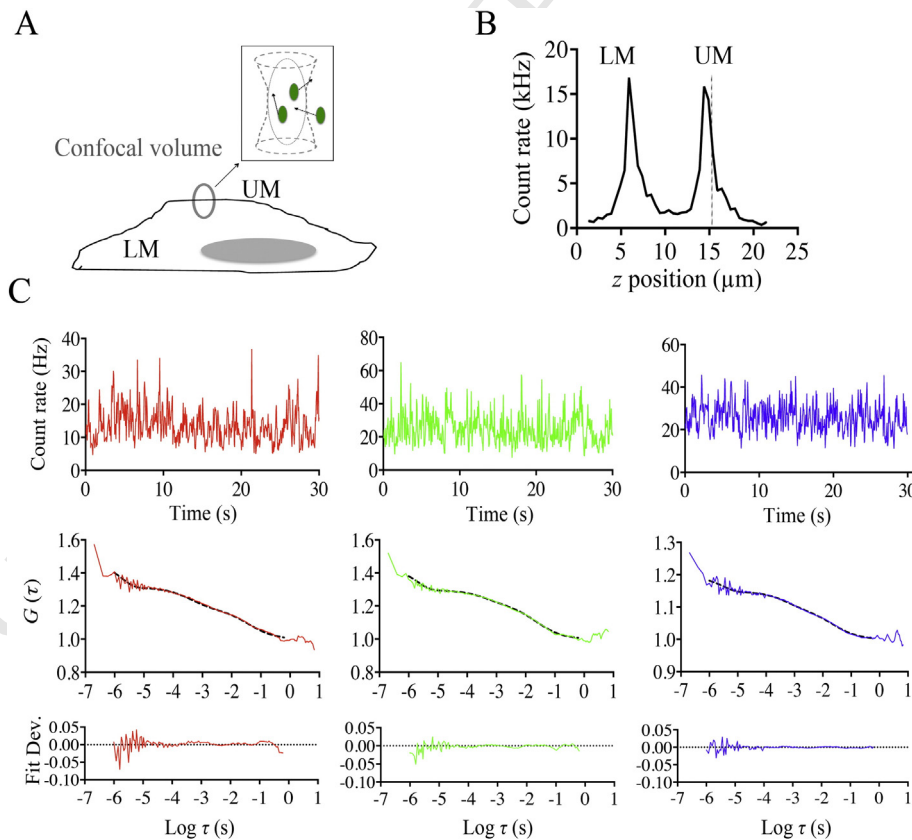


**Fig. 3.** Characterisation of the membrane dynamics of ABCG2 using fluorescence correlation spectroscopy (FCS). (A) Prior to FCS measurements, the confocal volume was positioned at the upper plasma membrane (UM) of the HEK293T cell to measure the fluctuations of the fluorescent molecules (green) in the plasma membrane, within the confocal volume. (B) A vertical scan (z-scan) was first performed to reveal the fluorescence intensity (count rate, kHz) peaks for the UM and lower plasma membrane, LM and the confocal volume was positioned at the peak corresponding to the UM. (C) Fluorescence intensity fluctuations recorded over time were analysed using autocorrelation models (Section 2.3) and examples of raw FCS traces and autocorrelation curves from GFP-ABCG2 (red), CD28-GFP (green) and CD86-GFP (blue) expressing cells were shown along with the fit deviation of the model.

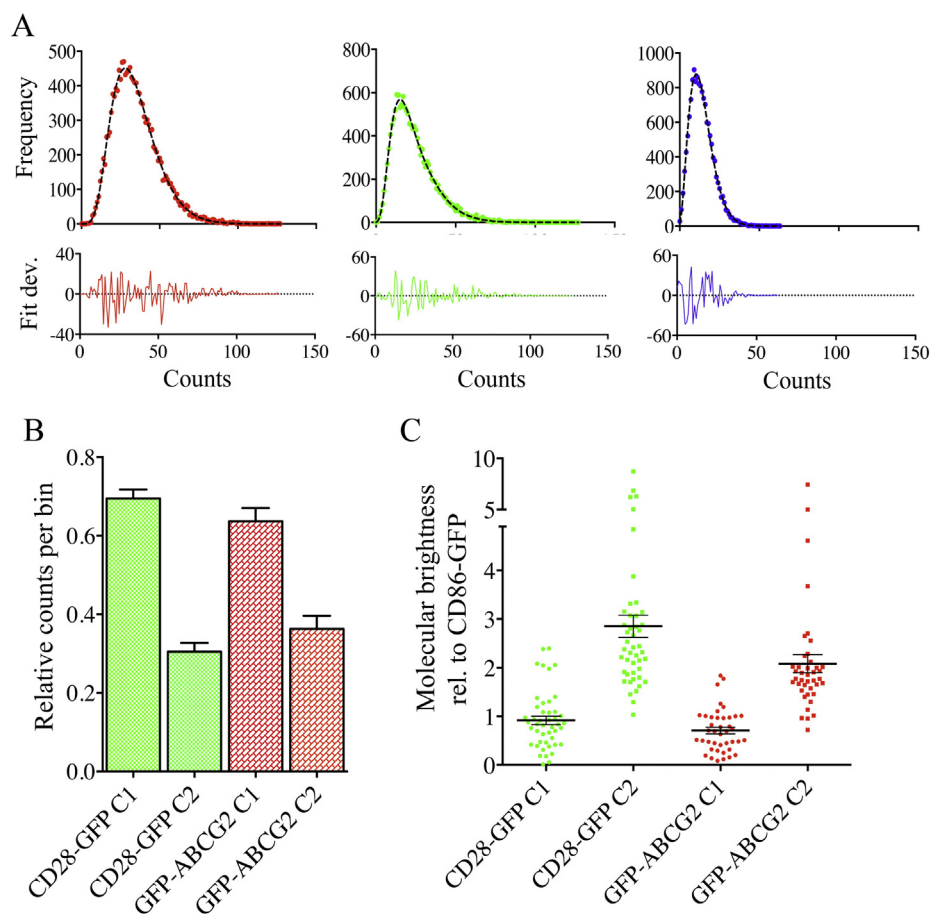


**Fig. 4.** PCH brightness analysis in live cells demonstrates oligomerisation of ABCG2 and CD28. (A) Examples of one-component model fitting (dotted curve) of PCH distribution obtained for CD86-GFP (blue, right panel) and two-component PCH model fitting (dotted curve) of PCH distribution obtained for GFP-ABCG2 (red, left panel) and CD28-GFP (green, middle panel). (B) Relative component fractions of component 1 (C1) and component 2 (C2) for CD28-GFP and GFP-ABCG2 determined from two-component PCH analysis, while (C) indicates the corresponding molecular brightness ratios of C1 and C2 obtained for CD28-GFP and GFP-ABCG2, relative to the molecular brightness of CD86-GFP obtained during the same experiment. PCH data were collected from at least 30 cells over 4 independent experiments.

distribution within this histogram deviates from an expected Poissonian in a manner which depends on the number and molecular brightness of the fluorescent particles within the confocal volume. As indicated in Fig. S2, a single component PCH model was sufficient to describe data from cytoplasmic GFP, and tandem GFP-GFP controls, and as expected, molecular brightness measurements differed by 1.86 fold ( $\epsilon = 8506 \pm 145 \text{ cpm s}^{-1}$  for GFP compared to  $15,809 \pm 484 \text{ cpm s}^{-1}$  for GFP-GFP; at least 25 cells, 3 experiments). A single component model was also most appropriate to describe the CD86-GFP data set ( $\epsilon = 12,828 \pm 889 \text{ cpm s}^{-1}$ ), in line with the prediction of a predominantly monomeric transmembrane protein (Fig. 4A).

However the PCH histograms derived from CD28-GFP and GFP-ABCG2 expressing cells required the assumption of two particle populations of differing brightness (components C1 and C2; Fig. 4B and C), as determined by reduced  $\chi^2$  comparison with the one-component model (Fig. S3). Two-component PCH analysis revealed that the second component, C2, identified for CD28-GFP and GFP-ABCG2 accounted for ~30% of the total particles (Fig. 4B), whereas this method did not reveal a second fluorescent species in CD86-GFP (Fig. S3). Molecular brightness values for C1 and C2 components of CD28-GFP and GFP-ABCG2 were normalised against the average  $\epsilon$  of CD86-GFP acquired on the same day (Fig. 4C). Component 1 (C1) brightness values for CD28-GFP and GFP-ABCG2 were similar to that of CD86-GFP ( $\epsilon$  ratios of 0.9 and 0.7, respectively; Fig. 4C), whilst the C2  $\epsilon$  measurements of CD28-GFP and GFP-ABCG2 were 2–3 fold higher than CD86-GFP, indicating that this component represented oligomers of fluorescent species (Fig. 4C). Furthermore, C2: C1 ratios for CD28-GFP and GFP-ABCG2, calculated

on the basis of paired individual measurements, were  $3.9 \pm 0.4$  and  $4.0 \pm 0.4$  respectively. Thus ABCG2 and CD28 C2 particle complexes appear to represent tetramers of the “unit” particles identified by C1. Assuming this unit particle represents the monomers of ABCG2 and CD28, then the “molecular ratios” calculated using the component fractions (Fig. 4B) and the C2: C1 “fluorescence ratios” suggest that approximately 69% of ABCG2 and 63% of CD28 molecules form tetrameric complexes.

### 3.4. Tetrameric organisation of ABCG2 is also indicated by single particle imaging and stepwise photobleaching analysis

PCH analysis thus provided quantitative measurement of the brightness of the fluorescent ABCG2 and CD28 species, from which the presence of oligomers, and their potential stoichiometry, could be inferred. However these measurements, while attributed to single particles, are inferred indirectly from statistical analysis and there are limitations to the fitted models – for example, in unambiguously resolving more than two components within a heterogeneous membrane population. To obtain further evidence for ABCG2 oligomerisation, TIRF imaging of individual lower plasma membrane fluorescent particles was performed, in combination with stepwise photobleaching analysis. This analysis was carried out on fixed cells, from the same low expressing clones used for FCS, to immobilise the fluorescent spots, which allowed their improved automated detection by avoiding the need for tracking movement over time [39]. Both GFP-ABCG2 and CD28-GFP expressing cells could be investigated using this method; however single membrane fluorescent spots in CD86-GFP cell lines were not resolved by



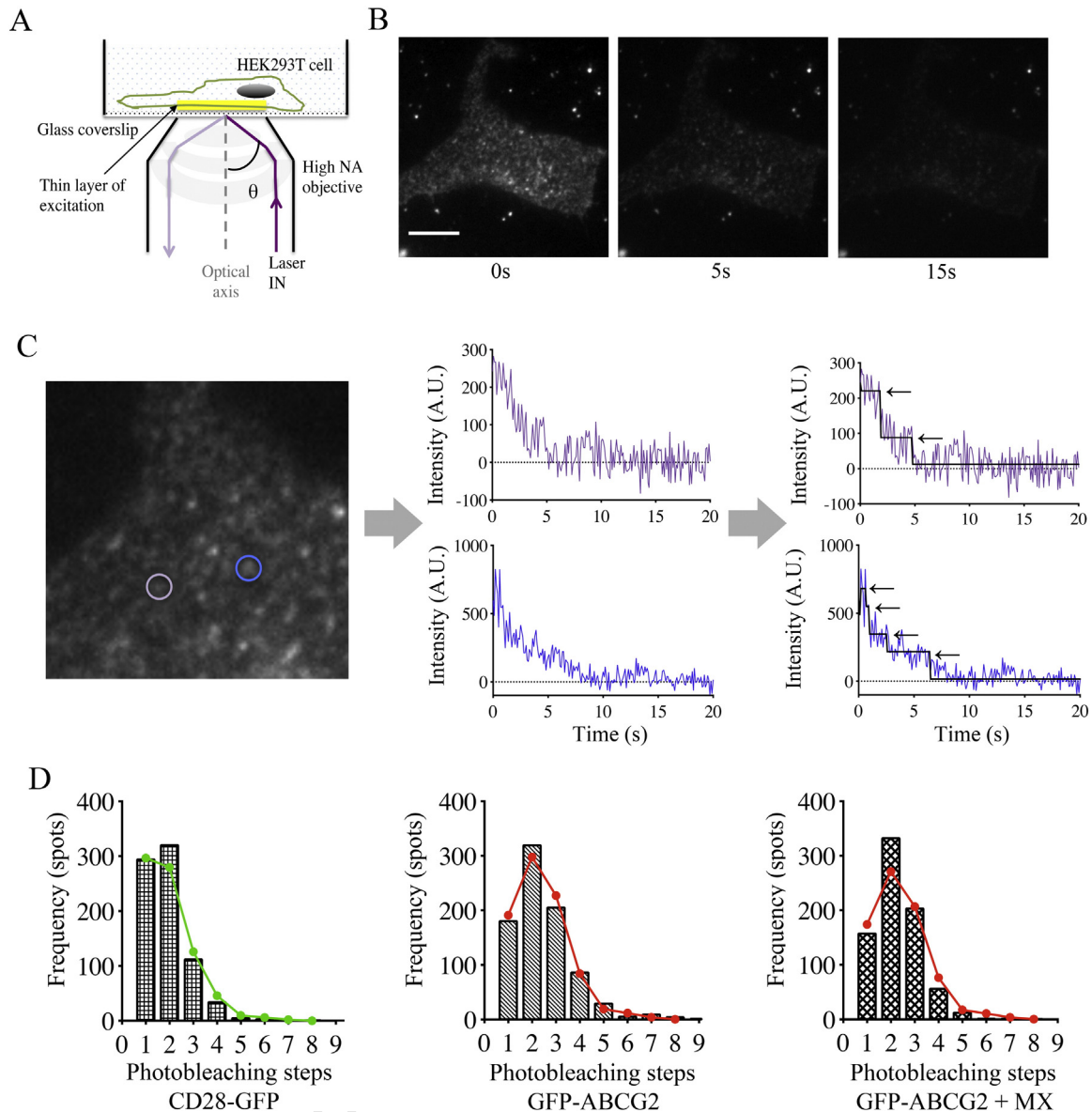


**Fig. 5.** Single particle TIRF imaging and stepwise photobleaching analysis reveals that ABCG2 forms tetramers. (A) A thin layer of excitation (yellow) in the lower membrane of HEK293T cell in aqueous medium was obtained through the generation of an evanescent field during total internal reflection. Laser excitation arrives at the glass-aqueous interface at a large angle ( $\theta$ ) and is reflected back into glass, instead of propagating through the aqueous medium or the sample. This phenomenon was achieved using high numerical aperture (NA) objective, NA of 1.45, and positioning the excitation laser away from the optical axis. (B) The lower membrane of HEK293T cells expressing GFP-ABCG2 at low levels was illuminated using TIRF configuration and photobleached at high power laser, recording video images at 10 Hz throughout. Complete photobleaching was observed after 15 s. (C) Stepwise photobleaching analysis of the TIRF video in (B) using the PIF algorithm [21], in which the fluorescent spots are first detected (left panel) and their fluorescence intensity traces calculated (middle panel). Photobleaching steps were finally determined using an iterative process (right panel). Frequency histograms (D) were then determined from pooled data for CD28-GFP, GFP-ABCG2, and GFP-ABCG2 cells pre-treated with substrate 4  $\mu$ M mitoxantrone for 30 min prior to fixation. These were fitted with dimer/tetramer models accounting for equal portion of dimers and tetramers (CD28; green curve, D), or 10% dimers and 90% tetramers (ABCG2; red curves, D). At least 30 cells were analysed over 5 (CD28, ABCG2 control), or 4 (ABCG2 incubated with MX) independent experiments.

441 TIRF (even at low expression levels), and this control was not considered further. TIRF imaging was first used to define individual fluorescent spots on the lower membrane (Fig. 5A), and a cell expressing GFP-ABCG2 is shown as a representative example (Fig. 5B; Supplementary Movie 1). During acquisition cells were photobleached with high power laser under TIRF configuration (Fig. 5B), and these videos over time were analysed using a fully automated spot detection algorithm developed previously [21] with the entire cell, and all associated spots, selected as the region of interest. Fluorescence intensity traces associated with individual spots (corrected for background) decayed in a series of discrete steps, interpreted as the successive bleaching of individual fluorescent GFP molecules within the particle complex (Fig. 5C). The algorithm accepted traces for analysis (see 2.6) and

454 identified the number of photobleaching steps within each trace in an unbiased manner. 455

456 Data representing all accepted spots from CD28-GFP or GFP-ABCG2 experiments were then pooled as step frequency histograms (Fig. 5D). 457 Rather than showing a unique step number, these histograms demonstrated a range of different photobleaching step frequencies, as previously reported for other membrane proteins [19,23]. This variation 458 can be attributed to at least three influences. Firstly, the presence of 459 non-fluorescent GFP molecules within the oligomeric complex (e.g. those forced into a dark state following high power laser excitation 460 used for TIRF) will lead to fewer than expected bleaching steps for any given complex stoichiometry. Second, the presence of any overlapping 461 fluorescent spots that are unresolved by the automated detection will 462 463 464 465 466



overestimate bleaching steps and stoichiometry. Finally it is also possible, indeed likely, that the CD28 and ABCG2 may exist as multiple populations with differing oligomeric states.

For the purpose of obtaining analysis that remained robust, modelling the photobleaching step histogram data was restricted to considering a homogenous population with a single stoichiometry, or two discrete oligomeric states in varying proportions. In both cases a binomial distribution was employed to account for the presence of non-fluorescent GFP molecules may be present within the complex. This distribution assigned a probability ( $p_{\text{GFP}}$ ) that individual GFP molecules contained within these complexes are fluorescent (see 2.6; [21]), with an optimised  $p_{\text{GFP}}$  of 0.55 (Fig. S4; Table 1). Of the single and dual component models that were considered, a dimer: tetramer model best described the CD28-GFP histograms, with an  $p_{\text{GFP}} = 0.55$  and equal (1: 1) proportions of dimer: tetramer particles (Fig. 5D, Table 1). To account for the low number of traces with more than four bleaching steps, the model also assumed that 10% fluorescent particles overlapped; alternatively this assumption could be interpreted as a minor population of higher order CD28-GFP complexes. The same dimer: tetramer model ( $p_{\text{GFP}} = 0.55$ , 10% spot overlap) was then optimised for the GFP-ABCG2 data. This demonstrated that in contrast to CD28-GFP, ABCG2 was organised predominantly as a tetramer (90%), with only a minority dimer population indicated (10%, Fig. 5D; Table 1). The distribution of GFP-ABCG2 photobleaching step frequencies did not change following treatment with substrate mitoxantrone (Fig. 5D; Table 1).

#### 4. Discussion

The relationship between structural organisation and function in the ABCG transporters has proved problematic due to their nature as “half transporters” – with a single NBD and TMD assumed to be insufficient for substrate export, compared to other members of the ABC

family [3,4]. In this study we resolved tetrameric organisation of ABCG2 complexes in whole cell membranes for the first time, using two complementary fluorescence approaches. This provides the essential basis for exploration of both ABCG2 function, and novel pharmacological approaches to target transporter oligomerisation and combat the development of multidrug resistance associated with overexpression of this transporter.

The advantages of our fluorescent approaches to examine ABCG2 distribution in intact cell membranes are highlighted by previous studies, which have presented mixed evidence for the ABCG2 oligomeric state. Although a dimeric functional unit for ABCG2 was suggested by some [5,40], others have proposed higher order ABCG2 stoichiometry [6,7]. Additionally, a previous electron microscopy study, using purified ABCG2 protein samples, suggested that tetrameric organisation was one oligomeric form of ABCG2, amongst others [41]. These studies were limited by the use of purified proteins, and/or the use of non-mammalian expression systems, e.g. baculovirus [6]. Furthermore, oligomeric organisation could be affected by the process of protein extraction or experimental conditions [7]. In contrast, we have investigated oligomerisation of ABCG2 in living or fixed non-polarised HEK293T cells (although ABCG2 is also expressed in some polarised cell types). We have presented evidence of tetrameric organisation of ABCG2, and reinforced these observations by the contrast with key controls such as the monomeric transmembrane protein CD86 in PCH analysis, and assessment of CD28 oligomers. A fluorescence recovery after photobleaching study suggested that CD28 is an obligate dimer [34], and this was supported in our stepwise photobleaching analysis through observation of an increased proportion of dimers, compared to tetramers, in the fitted model compared to ABCG2. Nevertheless, both PCH and TIRF photobleaching methods indicated higher order stoichiometry for CD28 as well, as suggested by others [36,42]. Furthermore, removal of the intermolecular disulphide interactions responsible for formation of CD28 dimers does not disrupt its oligomerisation [43], indicating the existence of plausible additional interactions that might contribute to higher order CD28 stoichiometry as well as dimers.

The use of two advanced fluorescence techniques strengthens our assessment of ABCG2 stoichiometry, because each has different strengths and weaknesses. PCH analysis allowed oligomerisation of ABCG2 to be demonstrated in plasma membrane of living mammalian cells, through the increase in molecular brightness when compared to the monomeric control CD86. Tandem GFP-GFP and GFP cytoplasmic controls (Fig. S2) illustrated the feasibility of this technique in identifying the direct relationship between brightness and the stoichiometry of the diffusing fluorescent protein complex. Furthermore, our conclusions derived from PCH for the more complex transmembrane fluorescent proteins rely on reasonable assumptions, such as that the  $\epsilon$  of component 1, and of the CD86 control, indeed relate to a monomeric unit, in agreement with the published literature for this protein (Fig. S3). Modelling of the super Poissonian PCH distribution is also limited to a realistic maximum of two components to define a heterogeneous underlying fluorescent protein population, and the behaviour of individual particles is statistically inferred, rather than directly observed using this technique.

In contrast, stepwise photobleaching analyses particles which are resolved as individual entities by TIRF. In this case fixed cells were required, as immobile fluorescent particles were preferred for the automated photobleaching analysis [34], which conferred more objective assessment of the photobleaching steps. This technique also required a key assumption that not all GFP molecules present in an ABCG2 complex under these experimental conditions were fluorescent, modelling this probability ( $p_{\text{GFP}}$ ) as 0.55. This agreed well with equivalent studies reported elsewhere [21,44], though higher maturation rates have been reported for oocyte expression systems [19,23]. Dependent on illumination conditions, a fraction of GFP molecules exist in a dark state [19], while quenching of fluorophores caused by changes in microenvironment (e.g. pH) or fixation, could contribute to a proportion of non-

**Table 1**

Goodness of fit assessment to determine the best fit binomial oligomeric models. The best models (Fig. 5, main text) were determined after a sequential goodness of fit analysis using  $\chi^2$  calculations. (A) Single oligomeric model analysis revealed that a tetramer (4-component) and a trimer (3-component) binomial models, accounting for 55% of fluorescent GFP molecules ( $p_{\text{GFP}} = 0.55$ ), best described the GFP-ABCG2 and CD28-GFP frequency histograms respectively, in which the lowest combined  $\chi^2$  were observed, suggesting that the binomial models of  $p_{\text{GFP}} = 0.55$  with 4-component or less can be used to describe the frequency histograms. (B) As ABCG2 and CD28 are known to form minimum complex of dimers, combined dimer/tetramer models with varying dimer: tetramer ratios were calculated to describe the frequency histograms. The best-fit dimer/tetramer models were determined using the lowest  $\chi^2$  obtained (highlighted in bold).

A			
<b>When <math>p_{\text{GFP}} = 0.50</math></b>			
Dimer model	GFP-ABCG2	CD28-GFP	
	1162	254	
Trimer model	83	4	
Tetramer model	10	20	
Pentamer model	10	57	
<b>When <math>p_{\text{GFP}} = 0.55</math></b>			
Dimer model	GFP-ABCG2	CD28-GFP	
	850	180	
Trimer model	52	<b>5</b>	
Tetramer model	<b>6</b>	39	
Pentamer model	27	101	
<b>When <math>p_{\text{GFP}} = 0.60</math></b>			
Dimer model	GFP-ABCG2	CD28-GFP	
	638	128	
Trimer model	34	13	
Tetramer model	12	70	
Pentamer model	56	169	
B			
Dimer:Tetramer (%)	CD28-GFP <sub>1</sub>	GFP-ABCG2 <sub>2</sub>	GFP-ABCG2 + MX
75:25	97	7	58
50:50	31	<b>2</b>	19
25:75	9	12	6
10:90	<b>5</b>	25	<b>5</b>

fluorescent GFP [45–47]. These factors may explain why accounting for a GFP fluorescent probability was unnecessary in PCH analysis of the same GFP-ABCG2 and CD28-GFP cell lines. In particular, the use of high power TIRF excitation to acquire and photobleach fluorescent particles would lead to a much greater proportion of dark state GFP molecules, compared to the conditions of low laser power acquisition used for FCS and PCH experiments. It was also necessary to consider various binomial models of oligomerisation when fitting the stepwise photobleaching frequency histograms (Table 1). Nevertheless, selection of the dimer: tetramer model was supported both statistically (Table 1) and by prior knowledge that ABCG2 and CD28 proteins can form dimers as a minimum functional unit [8,9,34]. Thus overall PCH demonstrated clear oligomerisation of ABCG2 and indicated potential tetrameric stoichiometry, whilst TIRF stepwise photobleaching analysis showed that ABCG2 tetramers were predominant.

The key questions that remain unanswered are the mechanisms by which ABCG2 forms tetrameric complexes and the extent to which this contributes to function. Indeed the relevance of tetrameric units might also be addressed more generally in the ABC transporter family, including the “full length” multidrug efflux pumps ABCB1 and ABCC1, which may still dimerise [48]. To our knowledge, there are no reliable mutations (within ABCG2) or compounds that can modify the oligomerisation of ABCG2. The ability to resolve ABCG2 stoichiometry in native cells using PCH and stepwise photobleaching techniques will therefore provide future impetus for exploring pharmacological manipulation of ABCG2 oligomerisation, and its consequences for transporter function.

Supplementary data to this article can be found online at <http://dx.doi.org/10.1016/j.bbamcr.2015.10.002>.

## Acknowledgements

KW was funded by a University of Nottingham PhD studentship. We thank Tim Self and colleagues in the School of Life Sciences Imaging unit (Nottingham) for technical assistance with FCS and TIRF, and Deborah Briggs and Marleen Groenen for molecular biology assistance. We thank Simon Davis (Oxford) for the gift of CD28 and CD86-containing plasmids and Rikard Blunck (Montreal) for assistance with the PIF algorithm. The authors are grateful to the Cell Signalling Research Group for useful discussions.

## References

- [1] G. Szakacs, J.K. Paterson, J.A. Ludwig, C. Booth-Genthe, M.M. Gottesman, Targeting multidrug resistance in cancer, *Nat. Rev. Drug Discov.* 5 (2006) 219–234.
- [2] C.F. Higgins, ABC transporters: from microorganisms to man, *Annu. Rev. Cell Biol.* 8 (1992) 67–113.
- [3] I.D. Kerr, A.J. Haider, I.C. Gelissen, The ABCG family of membrane-associated transporters: you don't have to be big to be mighty, *Br. J. Pharmacol.* 164 (2011) 1767–1779.
- [4] L.A. Doyle, W. Yang, L.V. Abruzzo, T. Krogmann, Y. Gao, A.K. Rishi, D.D. Ross, A multidrug resistance transporter from human MCF-7 breast cancer cells, *Proc. Natl. Acad. Sci. U. S. A.* 95 (1998) 15665–15670.
- [5] A. Bhatia, H.J. Schafer, C.A. Hrycyna, Oligomerization of the human ABC transporter ABCG2: evaluation of the native protein and chimeric dimers, *Biochemistry* 44 (2005) 10893–10904.
- [6] C.A. McDevitt, R.F. Collins, M. Conway, S. Modok, J. Storm, I.D. Kerr, R.C. Ford, R. Callaghan, Purification and 3D structural analysis of oligomeric human multidrug transporter ABCG2, *Structure* 14 (2006) 1623–1632.
- [7] J. Xu, Y. Liu, Y. Yang, S. Bates, J.T. Zhang, Characterization of oligomeric human half-ABC transporter ATP-binding cassette G2, *J. Biol. Chem.* 279 (2004) 19781–19789.
- [8] A.J. Haider, D. Briggs, T.J. Self, H.L. Chilvers, N.D. Holliday, I.D. Kerr, Dimerization of ABCG2 analysed by bimolecular fluorescence complementation, *PLoS One* 6 (2011), e25818.
- [9] Z. Ni, M.E. Mark, X. Cai, Q. Mao, Fluorescence resonance energy transfer (FRET) analysis demonstrates dimer/oligomer formation of the human breast cancer resistance protein (BCRP/ABCG2) in intact cells, *Int. J. Biochem. Mol. Biol.* 1 (2010) 1–11.
- [10] M.R. Arkin, Y. Tang, J.A. Wells, Small-molecule inhibitors of protein-protein interactions: progressing toward the reality, *Chem. Biol.* 21 (2014) 1102–1114.
- [11] R. Clark, I.D. Kerr, R. Callaghan, Multiple drug binding sites on the R482G isoform of the ABCG2 transporter, *Br. J. Pharmacol.* 149 (2006) 506–515.

- [12] S.J. Briddon, S.J. Hill, Pharmacology under the microscope: the use of fluorescence correlation spectroscopy to determine the properties of ligand-receptor complexes, *Trends Pharmacol. Sci.* 28 (2007) 637–645.
- [13] Y. Chen, J.D. Muller, P.T. So, E. Gratton, The photon counting histogram in fluorescence fluctuation spectroscopy, *Biophys. J.* 77 (1999) 553–567.
- [14] Y. Chen, L.N. Wei, J.D. Muller, Probing protein oligomerization in living cells with fluorescence fluctuation spectroscopy, *Proc. Natl. Acad. Sci. U. S. A.* 100 (2003) 15492–15497.
- [15] K. Herrick-Davis, E. Grinde, A. Cowan, J.E. Mazurkiewicz, Fluorescence correlation spectroscopy analysis of serotonin, adrenergic, muscarinic, and dopamine receptor dimerization: the oligomer number puzzle, *Mol. Pharmacol.* 84 (2013) 630–642.
- [16] G. Malengo, A. Andolfo, N. Sidenius, E. Gratton, M. Zamai, V.R. Caiola, Fluorescence correlation spectroscopy and photon counting histogram on membrane proteins: functional dynamics of the glycosylphosphatidylinositol-anchored urokinase plasminogen activator receptor, *J. Biomed. Opt.* 13 (2008) 031215.
- [17] A. Reiner, R.J. Arant, E.Y. Isacoff, Assembly stoichiometry of the GluK2/GluK5 kainate receptor complex, *Cell Rep.* 1 (2012) 234–240.
- [18] K. Nakajo, M.H. Ulbrich, Y. Kubo, E.Y. Isacoff, Stoichiometry of the KCNQ1 – KCNE1 ion channel complex, *Proc. Natl. Acad. Sci. U. S. A.* 107 (2010) 18862–18867.
- [19] M.H. Ulbrich, E.Y. Isacoff, Subunit counting in membrane-bound proteins, *Nat. Methods* 4 (2007) 319–321.
- [20] A. Demuro, A. Penna, O. Safrina, A.V. Yeromin, A. Amcheslavsky, M.D. Cahalan, I. Parker, Subunit stoichiometry of human Orai1 and Orai3 channels in closed and open states, *Proc. Natl. Acad. Sci. U. S. A.* 108 (2011) 17832–17837.
- [21] H. McGuire, M.R. Arousseau, D. Bowie, R. Blunck, Automating single subunit counting of membrane proteins in mammalian cells, *J. Biol. Chem.* 287 (2012) 65635912–35921.
- [22] W. Zhang, Y. Jiang, Q. Wang, X. Ma, Z. Xiao, W. Zuo, X. Fang, Y.G. Chen, Single-molecule imaging reveals transforming growth factor- $\beta$ -induced type II receptor dimerization, *Proc. Natl. Acad. Sci. U. S. A.* 106 (2009) 15679–15683.
- [23] K.O. Nagata, C. Nakada, R.S. Kasai, A. Kusumi, K. Ueda, ABCA1 dimer-monomer interconversion during HDL generation revealed by single-molecule imaging, *Proc. Natl. Acad. Sci. U. S. A.* 110 (2013) 5034–5039.
- [24] J.D. Pedelacq, S. Cabantous, T. Tran, T.C. Terwilliger, G.S. Waldo, Engineering and characterization of a superfolder green fluorescent protein, *Nat. Biotechnol.* 24 (2006) 79–88.
- [25] D.A. Zacharias, J.D. Violin, A.C. Newton, R.Y. Tsien, Partitioning of lipid-modified monomeric GFPs into membrane microdomains of live cells, *Science* 296 (2002) 913–916.
- [26] J.R. James, S.S. White, R.W. Clarke, A.M. Johansen, P.D. Dunne, D.L. Sleep, W.J. Fitzgerald, S.J. Davis, D. Klenerman, Single-molecule level analysis of the subunit composition of the T cell receptor on live T cells, *Proc. Natl. Acad. Sci. U. S. A.* 104 (2007) 17662–17667.
- [27] J.D. Allen, A. van Loevezijn, J.M. Lakhai, M. van der Valk, O. van Tellingen, G. Reid, J.H. Schellens, G.J. Koomen, A.H. Schinkel, Potent and specific inhibition of the breast cancer resistance protein multidrug transporter in vitro and in mouse intestine by a novel analogue of fumitremogin C, *Mol. Cancer Ther.* 1 (2002) 417–425.
- [28] S.J. Briddon, R.J. Middleton, Y. Cordeaux, F.M. Flavin, J.A. Weinstein, M.W. George, B. Kellam, S.J. Hill, Quantitative analysis of the formation and diffusion of A1-adenosine receptor-antagonist complexes in single living cells, *Proc. Natl. Acad. Sci. U. S. A.* 101 (2004) 4673–4678.
- [29] L.E. Kilpatrick, S.J. Briddon, N.D. Holliday, Fluorescence correlation spectroscopy, combined with bimolecular fluorescence complementation, reveals the effects of beta-arrestin complexes and endocytic targeting on the membrane mobility of neuropeptide Y receptors, *Biochim. Biophys. Acta* 1823 (2012) 1068–1081.
- [30] B. Huang, T.D. Perroud, R.N. Zare, Photon counting histogram: one-photon excitation, *Chemphyschem* 5 (2004) 1523–1531.
- [31] P. Macdonald, J. Johnson, E. Smith, Y. Chen, J.D. Mueller, Brightness analysis, *Methods Enzymol.* 518 (2013) 71–98.
- [32] C.A. Schneider, W.S. Rasband, K.W. Eliceiri, NIH image to ImageJ: 25 years of image analysis, *Nat. Methods* 9 (2012) 671–675.
- [33] S. Bhatia, M. Edidin, S.C. Almo, S.G. Nathenson, Different cell surface oligomeric states of B7-1 and B7-2: implications for signaling, *Proc. Natl. Acad. Sci. U. S. A.* 102 (2005) 15569–15574.
- [34] S. Dorsch, K.N. Klotz, S. Engelhardt, M.J. Lohse, M. Bunemann, Analysis of receptor oligomerization by FRAP microscopy, *Nat. Methods* 6 (2009) 225–230.
- [35] X. Zhang, J.C. Schwartz, S.C. Almo, S.G. Nathenson, Crystal structure of the receptor-binding domain of human B7-2: insights into organization and signaling, *Proc. Natl. Acad. Sci. U. S. A.* 100 (2003) 2586–2591.
- [36] M. Tacke, G. Hanke, T. Hanke, T. Hunig, CD28-mediated induction of proliferation in resting T cells in vitro and in vivo without engagement of the T cell receptor: evidence for functionally distinct forms of CD28, *Eur. J. Immunol.* 27 (1997) 239–247.
- [37] A. Aruffo, B. Seed, Molecular cloning of a CD28 cDNA by a high-efficiency COS cell expression system, *Proc. Natl. Acad. Sci. U. S. A.* 84 (1987) 8573–8577.
- [38] M.J. Saxton, Lateral diffusion of lipids and proteins, *Membrane Permeability 100 years since Ernest Overton*, Academic Press 1999, pp. 229–282.
- [39] R.J. Arant, M.H. Ulbrich, Deciphering the subunit composition of multimeric proteins by counting photobleaching steps, *Chemphyschem: a European journal of chemical physics and physical chemistry* 15 (2014) 600–605.
- [40] U. Henriksen, J.U. Fog, T. Litman, U. Gether, Identification of intra- and intermolecular disulfide bridges in the multidrug resistance transporter ABCG2, *J Biol Chem* 280 (2005) 36926–36934.
- [41] M. Dezi, P.F. Fribourg, A. Di Cicco, O. Arnaud, S. Marco, P. Falson, A. Di Pietro, D. Levy, The multidrug resistance half-transporter ABCG2 is purified as a tetramer upon selective extraction from membranes, *Biochim. Biophys. Acta* 1798 (2010) 2094–2101.

- 717 [42] J.L. Greene, G.M. Leytze, J. Emswiler, R. Peach, J. Bajorath, W. Cosand, P.S. Linsley, Co-  
718 valent dimerization of CD28/CTLA-4 and oligomerization of CD80/CD86 regulate T  
719 cell costimulatory interactions, *J Biol Chem* 271 (1996) 26762–26771.
- 720 [43] E. Lazar-Molnar, S.C. Almo, S.G. Nathenson, The interchain disulfide linkage is not a  
721 prerequisite but enhances CD28 costimulatory function, *Cell. Immunol.* 244 (2006)  
722 125–129.
- 723 [44] B. Coste, B. Xiao, J.S. Santos, R. Syeda, J. Grandl, K.S. Spencer, S.E. Kim, M. Schmidt, J.  
724 Mathur, A.E. Dubin, M. Montal, A. Patapoutian, Piezo proteins are pore-forming sub-  
725 units of mechanically activated channels, *Nature* 483 (2012) 176–181.
- 726 [45] N. Brewis, A. Phelan, J. Webb, J. Drew, G. Elliott, P. O'Hare, Evaluation of VP22 spread  
727 in tissue culture, *J. Virol.* 74 (2000) 1051–1056.
- [46] Y. Chen, J. Johnson, P. Macdonald, B. Wu, J.D. Mueller, Observing protein interactions  
728 and their stoichiometry in living cells by brightness analysis of fluorescence fluctu-  
729 ation experiments, *Methods Enzymol.* 472 (2010) 345–363.
- [47] S. Ganguly, A.H. Clayton, A. Chattopadhyay, Fixation alters fluorescence lifetime and  
731 anisotropy of cells expressing EYFP-tagged serotonin1A receptor, *Biochem. Biophys.*  
732 *Res. Commun.* 405 (2011) 234–237.
- [48] Y. Yang, Y. Liu, Z. Dong, J. Xu, H. Peng, Z. Liu, J.T. Zhang, Regulation of function by di-  
733 merization through the amino-terminal membrane-spanning domain of human  
ABCC1/MRP1, *J Biol Chem* 282 (2007) 8821–8830.

UNCORRECTED PROOF